J. Astrophys. Astr. (2019) 40:24
https://doi.org/10.1007/s12036-019-9592-3

Thermal shaping of thin glass panels for hard X-ray telescope optics

VINITA NAVALKAR[1,*], KULINDER PAL SINGH[2] and MEHERNOSH PRESS[3]

[1]Centre for Excellence in Basic Sciences, Vidyanagari Campus, Kalina, Santacruz (E), Mumbai 400 098, India.
[2]Indian Institute of Science Education and Research Mohali, Knowledge City, Sector 81, SAS Nagar, Punjab 140 306, India.
[3]Department of Physics, University of Mumbai, Mumbai 400 098, India.
*Corresponding author. E-mail: tifr.vinita@gmail.com

MS received 21 August 2018; accepted 12 May 2019; published online 15 June 2019

Abstract. We present a process for thermal forming of thin glass panels of borosilicate glass to produce mirror segments for X-ray telescope optics. The mirror segments are required to be shaped in a parabolic and hyperbolic shape in accordance with Wolter-I type design of X-ray telescope optics. Thermal forming of glass is a low-cost method to produce light-weight mirror segments. The process makes use of a semi-cylindrical quartz mold having surface roughness of the order of 1 nm. Flat glass sheets of 0.2 mm and 0.3 mm thickness are placed on the diametric edges of the mold. With a suitable thermal cycle, the glass sheets are thermally formed as per the shape of the mold. The shape of these formed glass sheets was measured using a non-contact optical setup. The surface quality measurements of the formed glass sheets were performed using atomic force microscope and they were found to be in the range of 0.04–0.33 nm. Once tested for acceptance, these glass sheets are coated using sputter deposition of multi-layers of high and low atomic number materials for hard X-ray reflection. Such mirror segments do not require polishing of the surface before being coated with multi-layers.

Keywords. Glass panels—multilayers—X-ray optics—X-ray telescopes.

1. Introduction

X-ray imaging telescopes for astronomy are based on the principle of grazing incidence, since the refractive indices for all known elements at X-ray wavelengths 100–0.1 Å or energies 0.1–100 keV are very close to unity. The Wolter-I configuration of the doubly reflecting optics (Figure 1) is widely used for X-ray telescopes that provide good sensitivity and imaging resolution. Such a design consists of a set of co-axial and con-focal shells of paraboloid and hyperboloid mirrors. X-rays are first reflected by an internally reflecting paraboloid mirror and then reflected to the prime focus of the telescope by the hyperboloid mirror. At grazing incidence angle α, the active region of the mirror is just a small fraction $(1/\alpha)$ of the mirror geometric area, giving a small collecting area. Therefore, several Wolter-I shells are usually nested co-axially to i increasing the reflecting areas (Figure 2) (Windt *et al.* 2009; Mao 2002; Mao *et al.* 1999; Singh 2005).

The segmented shells are used for optics because of their advantage of coupling light weight and low-cost designs in comparison with the monolithic mirrors of similar reflecting areas. The space-based X-ray astronomical telescopes like the ASCA (Tanaka *et al.* 1994; Aschenbach 2009), Suzaku XRT (Serlemitsos *et al.* 2007), XMM-Newton (Jansen *et al.* 2001), Swift XRT (Burrows *et al.* 2005), NuSTAR (Koglin *et al.* 2009), and the AstroSat SXT (Singh *et al.* 2015, 2016; 2017; Sagdeo *et al.* 2010) all use segmented mirrors as compared to the Chandra X-ray Observatory (Weisskopf *et al.* 2000) that uses monolithic mirrors. Thin aluminum foils or shells of nickel or glass sheets are considered to be good candidates to build a segmented optics with large effective areas and good angular resolution. The ASCA used thin foils of aluminum and carried four such telescopes each with 120 nested shells. This $\sim$420 kg observatory was the first example in which segmented conical foil mirrors were used for focusing X-rays. The reflectors of the Suzaku XRT were produced via a replication method consisting of 4 telescopes each

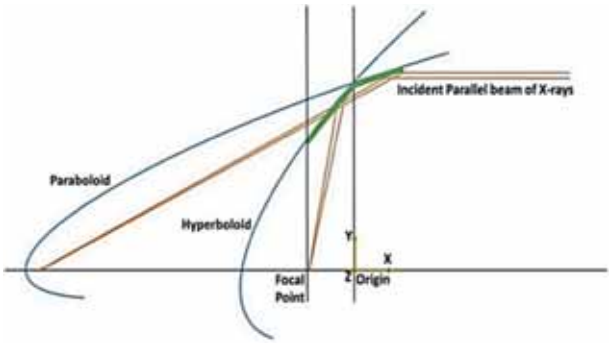

Figure 1. Wolter-I design for X-ray optics, showing a section of the paraboloid and the hyperboloid mirrors.

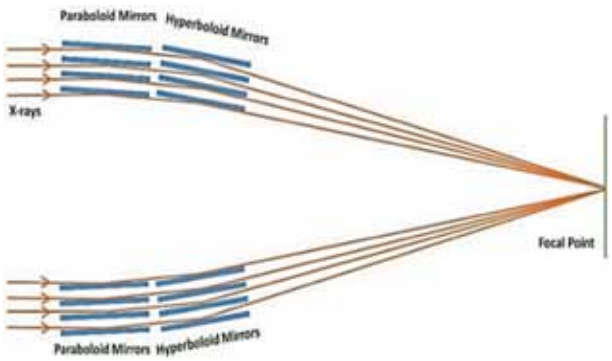

Figure 2. Ray diagram for focusing X-ray optics design using nested shells.

with 175 nested shells of foils in approximate Wolter-I geometry (Wolter 1961) for grazing incidence. The soft X-ray telescope (SXT) aboard the AstroSat (Singh 2015; Singh *et al.* 2014, 2016) employs focusing optics consisting of 40 concentric shells of conical foil mirrors of aluminum clad with replicated gold surfaces in an approximate Wolter-I configuration. NuSTAR also implements a similar design which consists of 133 concentric mirror shells of thin glass coated with Pt/SiC and W/Si multilayers.

NuSTAR optics operates in the energy range of 3–79 keV, whereas the other telescopes operate in the soft energy band of 0.3–8.0 keV. NuSTAR is the first X-ray telescope operating at high energies and represents the next generation of X-ray telescopes that will provide sensitivities ∼1000 times better than the non-focusing gas-filled proportional counters or the solid-state detectors (Ge-based) usually used for hard X-rays. The improved sensitivity is mainly due to the focusing of X-rays by the optics on a small part (a few pixels) of small size detectors, whereas the non-focusing systems depend on increasing the sensitive areas of the detectors, entailing a big increase in their mass (for example, RXTE (Jahoda *et al.* 1996), LAXPC (Agrawal *et al.* 2017) on AstroSat). The large mass of the detectors increases the interactions with charged particles and cosmic rays, thus increasing the internal background. The large field-of-view of such detectors also increases the external background, particularly at high energies. For example, in one unit of LAXPC (∼2000 cm^2 area and 1° field-of-view), the 10–79 keV background is ∼120 counts s^{-1} whereas a detection element with a radius of $2'$ in NuSTAR has a background of ∼0.03 counts s^{-1} in the same energy band (V. Chitnis, private communication) for optics with an area that is ∼10 times smaller. Therefore, we have initiated developments to realize the next generation of X-ray telescopes, like NuSTAR, in India which would work at hard X-ray energies up to 70 keV.

In this paper, we present the results of our experiments in realizing glass substrates using thermal-forming process. Since X-ray wavelengths are of the order of the distance between the atomic planes, therefore, the most demanding requirement for fabricating X-ray mirrors is to have low surface roughness. Surface roughness of the order of the X-ray wavelengths can scatter X-rays. Therefore, the value of RMS roughness, defined as the root mean square value of the scale heights of roughness on a surface should be less than 10 Å to have maximum specular reflectance and little scattering. The surface roughness is dependent on both the parameters of the substrate as well the quality of the reflecting materials deposited. In the case of the glass sheets that are thermally slumped to the required shape, it is observed that minor changes in the thermal-forming parameters can change the surface properties of the final mirrors. The material deposited on thermally-formed glass replicates the irregularities of the thermally-formed glass surface and even minor bumps on the surface serve as a seed for crystal growth around that region. The overall effect is the amplification of non-uniformities after deposition of a reflecting material.

This paper is arranged as follows: In Section 2, we present the underlying theory and physical properties involved in the process of glass slumping. In Section 3, we present the slumping process that we have followed. In Sections 4 and 5, we discuss the techniques used in our laboratory to measure the stress and shape of the slumped glass sheets, followed by surface roughness measurements in Section 6, and our conclusions is given in Section 7.

2. Physical properties of the glass sheets used in thermal forming

Viscosity plays an important role in determining the time required for forming and the final shape of the thermally-formed glass.

The viscosity of glass has a considerable effect on its other physical properties such as melting and crystallization characteristics and thus controls the temperature and pressure ranges within which the glass can be worked on. When high speed mass production techniques are employed, the glass must conform closely to viscosity tolerances so that products will have uniformity of thickness, shape and strength. Therefore, the knowledge of glass viscosity as a function of temperature and glass composition is crucial for efficient glass-forming process.

The most commonly used viscosity– temperature relationship for a wide span of viscosities (over 12 orders of magnitude) is the Vogel–Fulcher–Tammann (VTF) equation (Jimenez-Garate *et al.* 2003; Pye *et al.* 2005)

$$\eta\,(T) = \eta_0 \mathrm{e}^{\left(\frac{T_0}{T-T_\infty}\right)}, \tag{1}$$

where η_0, T_0 and T_∞ are independent constants and are obtained based on the values obtained from the datasheets for the Schott D263 T-Eco glass sheet used by us. The uniformity in thickness after forming can be achieved by minimizing. This rate depends on the materials present in the glass. More silica contents flatten the $\eta(T)$ curve, i.e. $\mathrm{d}\eta(T)/\mathrm{d}T$ becomes smaller for all T, whereas, the addition of alkali oxides gives the reverse effect. Using alumina instead of boric acid also steepens the curve (Jimenez-Garate *et al.* 2003; Pye *et al.* 2005).

The terms generally involved in the glass-forming stages are the *strain point*, the *annealing point*, and the *softening point* shown in Figure 3. They are defined by the viscosity values obtained empirically. The strain point is defined at $10^{13.5}$ Pascal-sec (Pa · s). At temperatures below the strain point, we can temporarily heat and cool the glass without introducing permanent stresses. The annealing point, defined at 10^{12} Pa·s, is the temperature at which the glass is stress relieved after 10 or 15 min. Above the thermal-forming temperature T_f, where $T_f = 10^{10}$ Pa · s, the bulk behavior is no longer elastic, and glass becomes a viscous fluid. The softening point is at $10^{6.6}$ Pa · s (Jimenez-Garate *et al.* 2003).

The surface tension is another factor that impacts the thermal-forming process of the softened glass. It plays a key role in flattening the thermally-formed glass surface by self-relaxation phenomena and is partly responsible for holding the thermally-formed glass in shape during slumping (Jimenez-Garate *et al.* 2003; Pye *et al.* 2005).

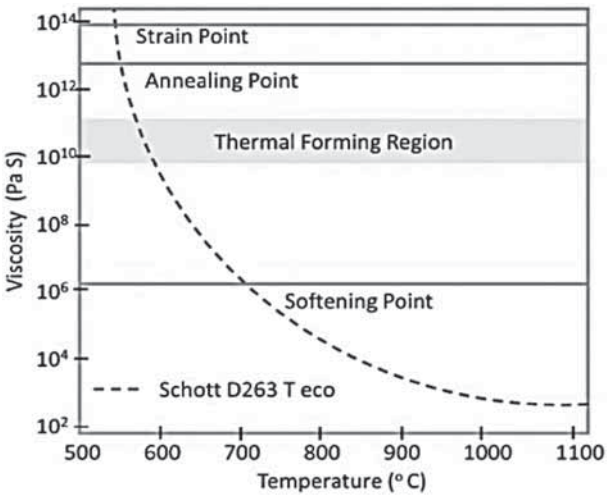

Figure 3. Viscosity vs. temperature for Schott D263 T Eco borosilicate glass (Jimenez-Garate *et al.* 2003; Schott 2013).

3. Thermal-forming process

Flat thin sheets of smooth borosilicate glass are thermally formed into semi-cylindrical shells using semi-cylindrical quartz mandrels. This process requires no fine polishing of the surface. A quartz mandrel (quartz having a higher melting point of 1200°C than borosilicate glass) acts like a guiding mold for the thin glass during thermal-forming process (Figure 4). The quartz mandrels used in the process have radius r ranging from 90 mm to 220 mm. The length L of all the mandrels used is 250 mm (Fig 4). The surface roughness of the used mandrels is of the order of 1 nm. Programmable furnaces are used to do multiple cycles of raising the temperature at a specified rate and then holding at that temperature for a specified time within the temperature range. We have used borosilicate Schott D263 T Eco of 0.2 mm and 0.3 mm thicknesses in this process.

The procedure adopted by us for the thermal-forming of glass sheets on the concave side of the quartz mandrel, is shown in Figure 4 and is described below (Jimenez-Garate *et al.* 2003)

- A rectangular cut piece of glass sheet is placed on top of the concave side of a semi-cylindrical shell quartz mandrel (Figure 4(b)). The width of the cut glass sheet

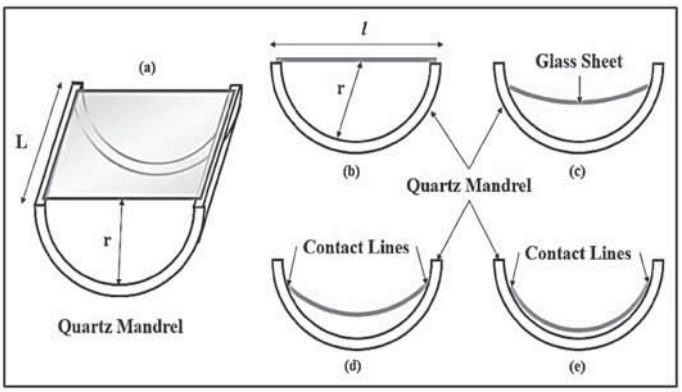

Figure 4. Cross-sectional schematic showing glass sheets in different stages in the thermal-forming process. The quartz mandrel which serves as a mold for glass sheet during the forming process.

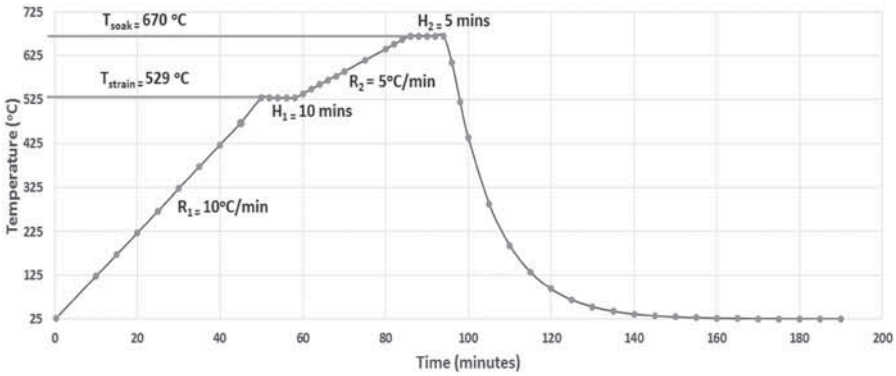

Figure 5. Curve obtained using a Vulcan 3–550 muffle programmable furnace for Schott D263 T Eco glass sheets.

is kept slightly larger than the inner diameter of the quartz mandrel.
- The quartz mandrel along with the glass sheet is then introduced into the programmable furnace.

First thermal cycle

- The furnace at room temperature T is ramped up at a rate of $R_1 = \mathrm{d}T/\mathrm{d}t = 10°\mathrm{C/min}$ to reach the strain temperature T_{strain} (Figure 5).
- After reaching the strain point, $T_1 = T_{\mathrm{strain}}$, the furnace is allowed to thermalize for H_1 minutes (Figure 5).

Second thermal cycle

- After thermalization, the temperature is again increased with a reduced ramped up rate $R_2 = \mathrm{d}T/\mathrm{d}t = 5°\mathrm{C/min}$ to reach the temperature $T_2 = T_{\mathrm{soak}}$ (Figure 5). At T_{soak}, the viscosity of the glass is $10^9 - 10^{10}$ Pa · s.
- By heating the glass above its strain point (around 550°C for D263 T Eco) and below its softening point (around 650°C for D263 T Eco), the stress-relieved glass forms under its own weight (Figure 4(c)). The glass viscosity is high enough that its thickness does not change appreciably during forming (Figure 3)
- When the furnace reaches the soak temperature, it is again allowed to soak for H_2 minutes. After the soak time H_2 (Figure 5) has elapsed, the furnace is shut down. The soak time H_2 is very crucial in defining the final surface properties of the thermally-formed glass. It is derived empirically (Table 1).
- The glass is annealed when it is allowed to cool slowly within the furnace, until well below the strain point (Figure 3).
- Figure 4(e) shows the final formed glass where only the lateral edges touch the quartz mandrel.

The parameters (Table 1) for forming process were finalized, based on the data obtained in AFM scanning (Table 2).

In the initial stage of developing standard procedure for thermal slumping, experiments were conducted using silicon cloth as a buffer between the glass sheet and the mandrel (Figure 6). Different thermal cycles were followed, and the surface properties of the formed glass sheets were studied using AFM data. The cloth

Table 1. Furnace settings for various thermally-formed glass sheets.

	Forming side						
	Concave side						Convex side
Sample No.	S71	S83	S89	S95	S99	S102	S105
Thickness (mm)	0.3	0.2	0.3	0.2	0.2	0.3	0.3
Si cloth	✓	✓	✘	✘	✘	✘	✘
R1 (°C/min)	10	10	10	10	10	10	10
R2 (°C/min)	5	5	5	5	5	5	5
R3 (°C/min)	–	–	5	5	–	–	–
T1 (°C)	529	529	500	500	529	529	529
T2 (°C)	670	670	580	580	670	670	670
T3 (°C)	–	–	670	670	–	–	–
H1 (min)	7	7	7	7	10	10	10
H2 (min)	4	4	4	4	5	5	5
H3 (min)	–	–	4	4	–	–	–

Table 2. AFM results for various thermally-formed glass sheets.

	Forming side							
		Concave side						Convex side
Sample No.	Flat glass	S71	S83	S89	S95	S99	S102	S105
No. of thermal cycles	–	2	2	3	3	2	2	2
Thickness (mm)	0.3	0.3	0.2	0.3	0.2	0.2	0.3	0.3
Si cloth	–	✓	✓	✘	✘	✘	✘	✘
Roughness average – Ra (nm)	0.058	0.083	0.10	0.096	0.081	0.045	0.030	0.021
Roughness RMS – Rq (nm)	0.075	0.102	0.13	0.123	0.104	0.058	0.038	0.036
Waviness average – Wa (nm)	0.258	0.164	0.500	0.194	0.198	0.148	0.098	0.102
Waviness RMS – Wq (nm)	0.325	0.173	0.640	0.252	0.183	0.165	0.108	0.116

caused local heating of the glass due to which minor bumps were observed on the glass surface (Figure 7). The cloth also left behind lint sticking to the glass, which was difficult to clean.

Slumping of glass was carried out on both convex and concave sides of the quartz mandrel. When the glass is formed on a concave surface, the surface that will reflect the X-rays never touches the mandrel. In this method, cooling is done just before the glass touches the base of the mandrel. Hence, the glass makes contact only with the mandrel at the lateral edges during the entire process (Figure 4(e)) acquiring nearly the shape of the mandrel. The formed glass shell is then cut at the lateral edges to eliminate edge deformations. On the other hand, when the glass is slumped on the convex side (Figure 8), the surface to be coated touches the side of the mandrel, which prevents it from developing local bumps on the surface. This can only be ensured with quartz mandrel machined with extremely good surface specifications. It also reduces the chances of contamination of the coating side surface in the furnace. In this process, the lateral edges of the thermally-formed glass remain flattened in comparison to the glass sheets formed on the concave side, which can later be cut off. In both the cases, thermally-formed glass sheets having surface roughness less than 2 Å were obtained (Figure 9). The quality improved marginally in terms of roughness and waviness when slumped on the convex side.

Either methods can be applied to achieve the final slumped glass sheets for the X-ray telescope optics. The choice of the method depends on the choice of the mandrels used or the furnaces used. Since the mandrels used

Figure 6. Initial experiments using a silicon cloth between the glass sheets and the mandrel to avoid adhesion of molten glass to the mandrel surface. This procedure was later discarded.

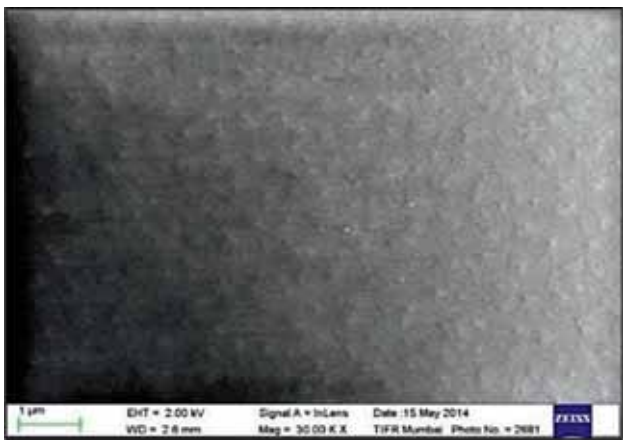

Figure 7. SEM image (1 μm spatial resolution) of the glass piece slumped with silicon cloth shows minor bumps formed on the surface due to local heating.

in our experiment were machined to 1 nm smoothness, it provided good surface specification to the slumped glass sheet. It also flattened any undesired bumps on the side which will be used for reflection.

The furnace used in the experiment has ceramic walls. These walls leave powdered dust particles on the surface of the samples. In case of the concave side, this dust gets directly deposited on the side which will be used for reflection. In case of the convex side, this effect can be minimized.

4. Stress measurement of thermally-formed glass sheets

It was observed in certain experiments, that the formed glass either cracked during the thermal-forming process

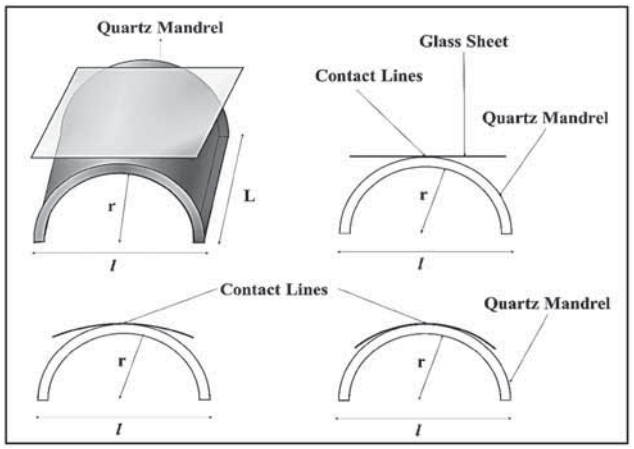

Figure 8. Cross-sectional schematic showing glass sheets in different stages in the thermal-forming process (on the convex side of the quartz mandrel). The quartz mandrels used in the process have radius r ranging from 90 mm to 220 mm. The length *L* of all the mandrels used is 250 mm.

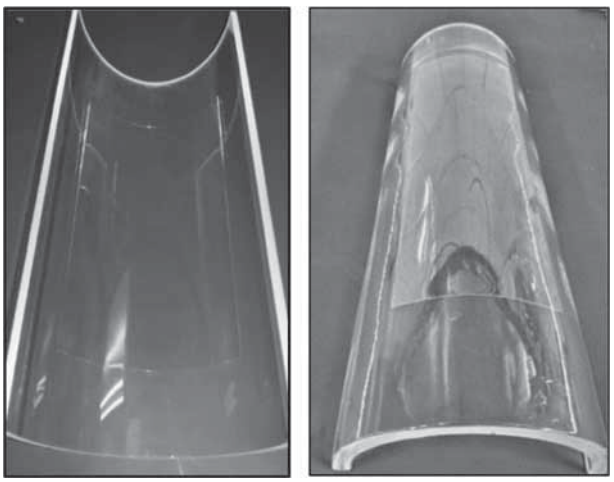

Figure 9. Images of the thermally-formed glass sheets on the concave side and the convex side of the quartz mandrel.

or during the sputtering process. This was due to the presence of residual stresses after the thermal-forming process. Tensile residual stresses can lead to crack growth and breakage. The stresses generally introduce micro cracks along the edges of the glass during thermal forming. These cracks are seen to propagate along the width of the glass and eventually fracture the entire structure. The stress on such glass sheets increases further due to the deposition of reflecting materials in the sputtering chamber, which leads to breaking of the glass.

Various stress measurement techniques have been developed to measure the residual stresses in the glass. One of them is the photo-elasticity method, which is

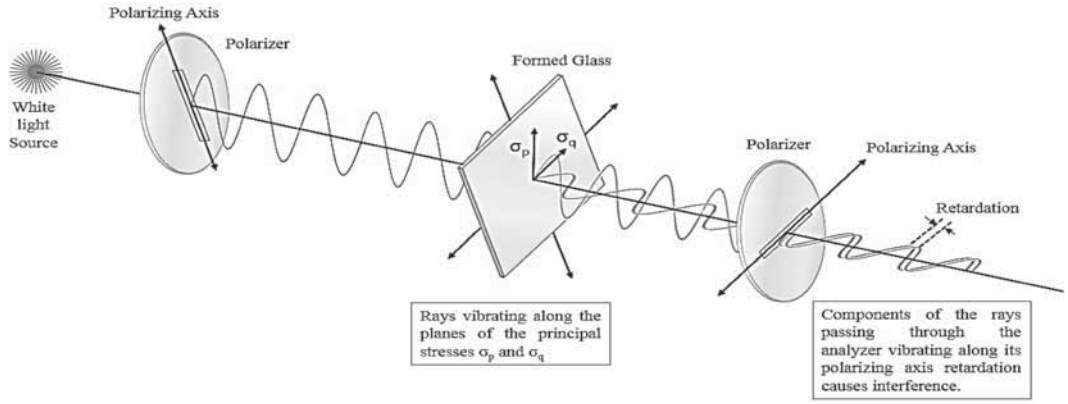

Figure 10. Polariscope setup to measure stress in thermally-formed glass.

a non-destructive and non-contact residual stress measurement technique. It serves as an important tool for determining the critical stress points in a material. Photo-elastic material such as borosilicate glass exhibit the property of birefringence only in the presence of stress. This birefringence is proportional to the magnitude of the residual stress. When a ray of light passes through the photo-elastic material, it gets polarized and gets resolved along the two principle stress directions and each of these components experiences different refractive indices. The difference in the refractive indices leads to the relative phase retardation between the two component waves. The magnitude of the relative retardation is given by the stress optic law (Wang 2010; Orr & Finlay 1997)

$$R = Ct\,(\sigma p - \sigma q)\,, \tag{2}$$

where R is the induced retardation, C is the stress optic coefficient, t is the specimen thickness, σ_p is the first principal stress and σ_q is the second principal stress. The two waves are then brought together in a polariscope, where they interfere and we get a fringe pattern depending on the relative retardation. Thus, by studying the fringe pattern, one can determine the state of stress at various points in the material.

A polariscope arrangement was setup using two polarizer sheets, a diverging lens and a source of white light (Figure 10). A total of 45 thermally-formed glass substrates were tested (40 substrates on the concave side and 5 substrates on the convex side). The results showed that only a few (only 9 formed on the concave side out of 45) substrates had residual stress in them. Most of the glass sheets formed were stress-free. To check at what point the glass sheets become stress-free, a few of them were cooled suddenly after the soak time. Such sheets cracked instantly to release stress. The coloured

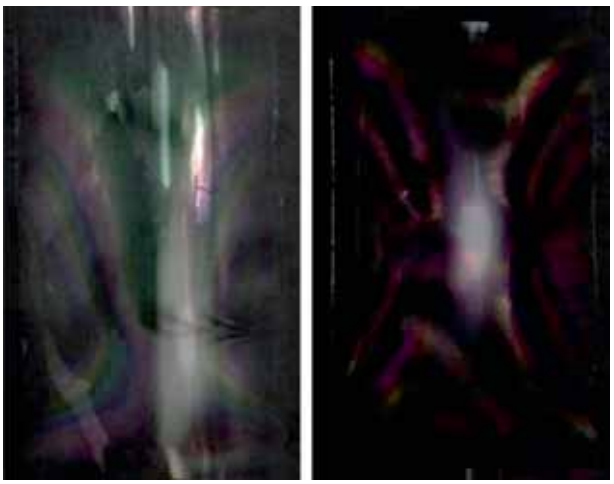

Figure 11. Two glass sheets thermally formed showing stress-induced birefringence.

patterns observed on the surface of the glass sheets (Figure 11) are due to birefringence indicating the presence of residual stress.

This method was used only for qualitative analysis of the stress in the formed glass sheets. The quantitative analysis requires a different apparatus setup. The relationship between interference color and birefringence patterns is graphically illustrated in the classical Michel–Levy interference color chart (Sørensen 2014).

5. Shape measurement of the thermally-formed glass sheets

In order to use the thermally-shaped glass as substrates for building X-ray optics, it is important to verify the

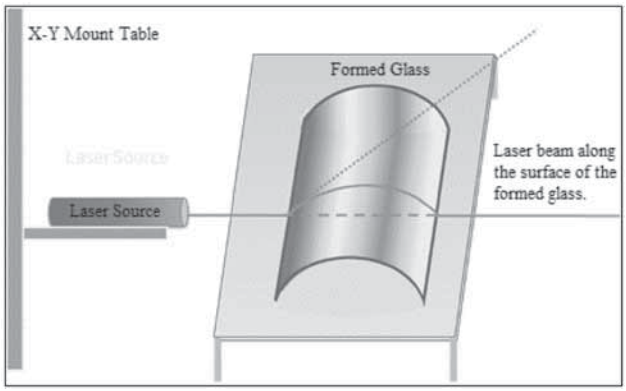

Figure 12. Experimental setup for measurement of curvature and shape of formed glass and the actual images.

Figure 13. Images obtained using the experimental setup shown in Figure 12.

figure of the formed glass sheets. Hence, a simple experiment was designed to conduct shape measurement of the formed glass sheets (Figure 12). The setup consisted of a laser source which was focused on to the lateral edges of the formed glass.

The laser beam was split into three rays: one tracing the path along the surface of the curved glass, one reflected at a certain angle at the lateral edges of the glass, and one along the straight line unobstructed (Figure 13). The rays along the surface of the curved glass were photographed for different samples removing the parallax (Figures 14, 15 and 16) and fitted using semicircle profile fit in MATLAB.

The blue semicircle in Figures 14, 15 and 16 show the fitted semicircle profile in MATLAB, whereas the red lines are the arcs obtained from photographs. The radius of the semi-circular fit was taken equal to the radius of the mandrel used.

6. Surface roughness measurements

The surface roughness characteristics for all the thermally-formed glass were measured using Atomic Force Microscope (AFM). Nanosurf NaioAFM - BT05164 was used in dynamic non-contact mode. It has a z-axis resolution of less than 1 Å in this mode,

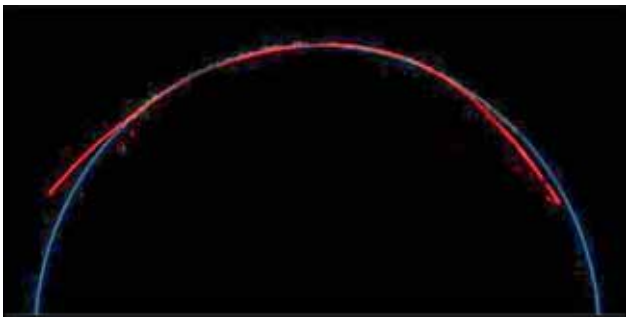

Figure 14. Slumped using three cycles of temperature raising on the concave side of the quartz mandrel. The radius of curvature is 90 mm.

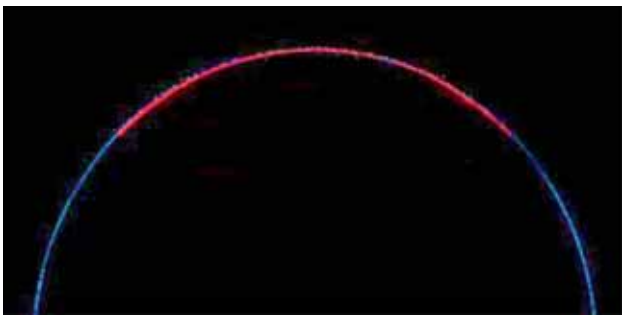

Figure 15. Slumped using two cycles of temperature raising on the concave side of the quartz mandrel. The radius of curvature is 90 mm.

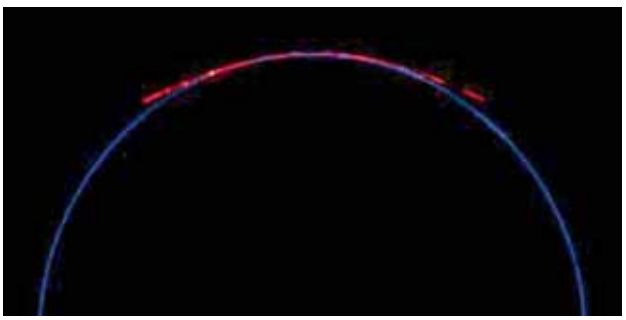

Figure 16. Slumped using two cycles of temperature raising on the convex side of the quartz mandrel. The radius of curvature is 92 mm.

operated by allowing an extremely fine sharp cantilever tip to vibrate in very close proximity to the sample that is being imaged. The cantilever (Tap 190AI-G-10) used for measurement has a resonance frequency of 190 kHz in a range of 130–250 kHz and dimensions of 225 x 38 μm. The forces most commonly associated with atomic force microscopy are interatomic van der Waals forces.

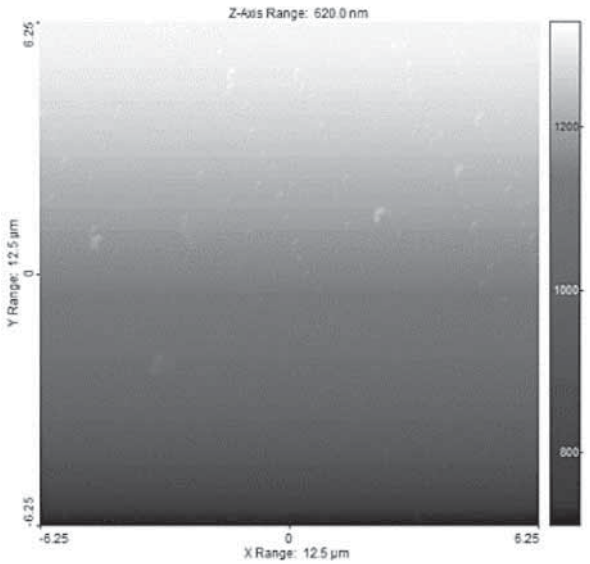

Figure 17. 2D scanned image plots of Sample S71.

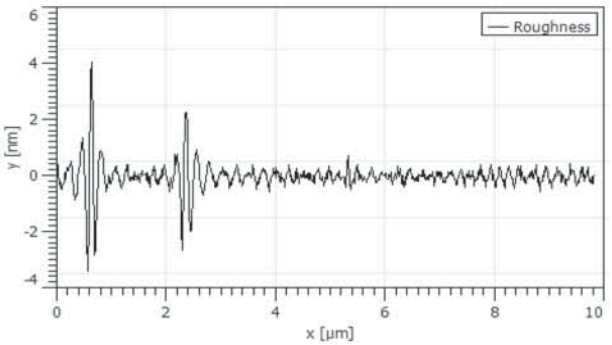

Figure 18. Roughness line profile for Sample S71.

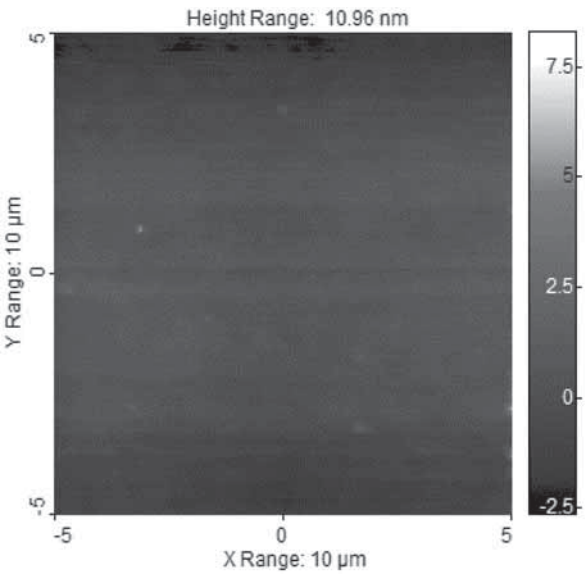

Figure 19. 2D image plots of Sample S83.

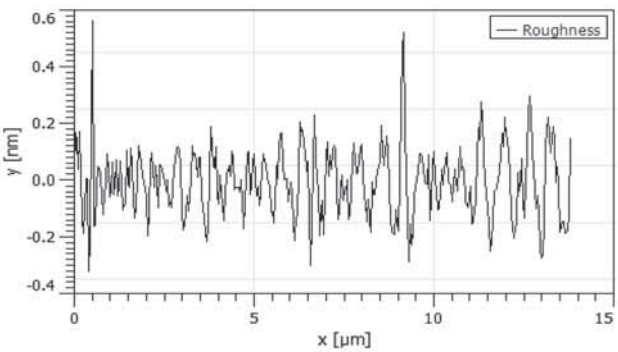

Figure 20. Roughness profile for Sample S83.

Each glass sample was scanned at different points and the average surface roughness and waviness profiles were extracted A flat glass panel was considered as a reference for qualitative analysis of all the samples. Samples S71 and S83 were slumped using silicon cloth between the glass and the quartz mandrel. The thermal-forming parameters of all the samples mentioned below are given in Table 1.

The average roughness R_a is the area between the roughness profile and its mean line or is defined as the integral of the absolute value of the roughness profile height over the evaluation length. The root mean square R_q is the square root of the average of the square of the deviation of the profile from the mean line. This parameter is more sensitive to the peaks and valleys than R_a. The RMS surface roughness for all the samples (total 13 scanned in AFM) was in the range of 0.03–0.15 nm and the RMS waviness of the formed glass sheet was in the range of 0.10–0.65 nm (Table 2). Sample S105 was slumped on the convex side of the quartz mandrel.

The 2D scanned image plots and roughness profiles for some of the samples are shown in Figures 17, 18, 19, 20, 21, 22, 23, 24, 25 and 26. They are extracted from the AFM data using Gwyddion Analysis Software.

To summarize the results shown in Table 2, we find that, Samples S99 and S102 show significant improvement over Samples S71 and S83. Samples S71 and S83 were thermally formed using a silicon cloth. As discussed in Section 3 (Figure 7), glass sheets slumped in this process had tiny silicon cloth threads (lint) sticking to it. These lints introduced undesired roughness and waviness to the glass surface.

In the process of thermal forming described in this paper, the glass is not allowed to reach the melting

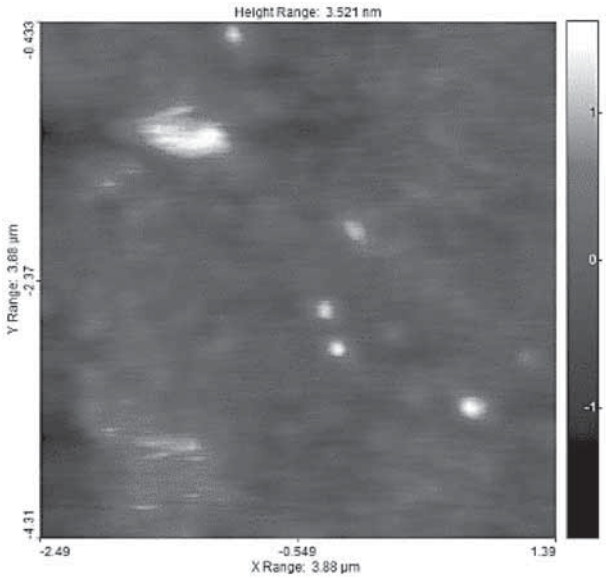

Figure 21. 2D image plots of Sample S95.

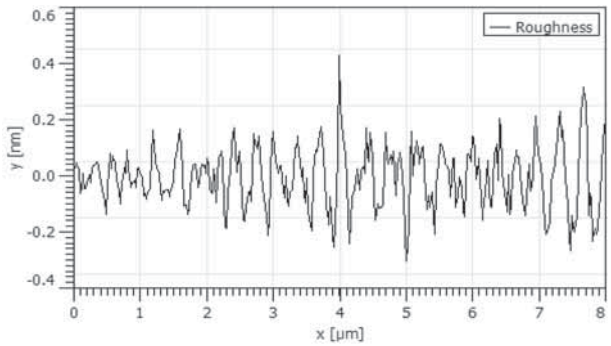

Figure 22. Roughness profile for Sample S95.

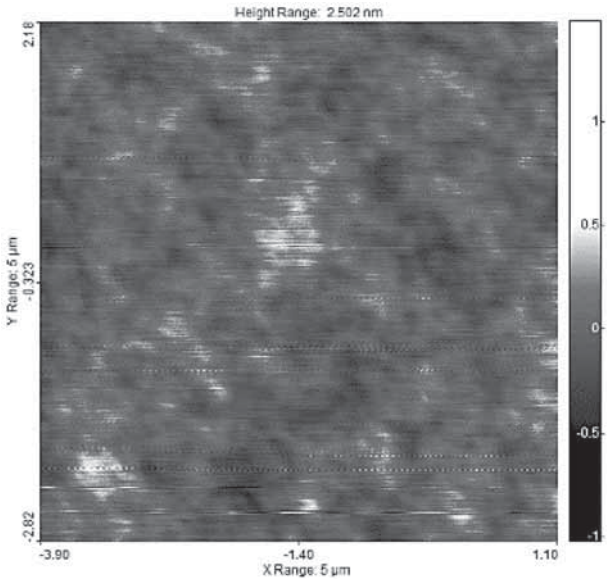

Figure 23. 2D image plots of Sample S99.

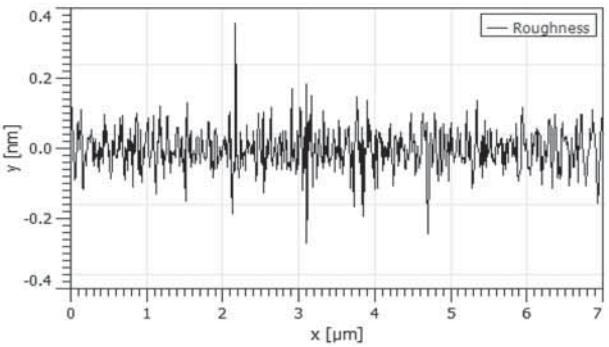

Figure 24. Roughness profile for Sample S99.

point. Annealing is done just before the glass reaches the melting point. At the annealing point, the glass is soft enough for stress relaxation within several minutes. This ensures that the thickness of the glass does not change, and the glass sheet takes the final shape under its own weight. For Samples S83, S95 and S99, 0.2 mm thin glass sheets were used. Though fairly good results were obtained in Sample S99, 0.2 mm glass is too thin to sustain all the stresses that are introduced after the deposition of multilayers of X-ray reflective coating material. Hence it was discarded.

Samples S89 and S95 were formed using three thermal cycles. It was observed that the surface roughness of these samples is close to 1 Å, but the waviness is high. One possible reason for this can be the rate of change of temperature R_3 (Table 1) and the soak time H_2 (Table 1). For the glass in use (D 263 T Eco), the transition region or the thermal-forming region is defined to be between 500 °C to 600 °C. In this region, if the glass is subjected to a sudden variation in temperature (R_3), a molecular re-arrangement occurs in the structure. This process is called structural relaxation. This can possibly explain the high waviness seen in the sample. Also, soak time H_2 is very crucial in defining the final surface properties of the thermally-formed glass. Glass being a bad conductor of heat, a temperature gradient will be present on the surface of the formed glass if the soak time H_2 is small. A high soak time H_2 will delay the annealing process, which will introduce stress and variation in the thickness of the glass sheets due to melting. This may also lead to the central region of the formed glass to touch the mandrel. The final value for soak time H_2 has been found empirically. It was observed that annealing of the glass is very sensitive to the soaking time H_2.

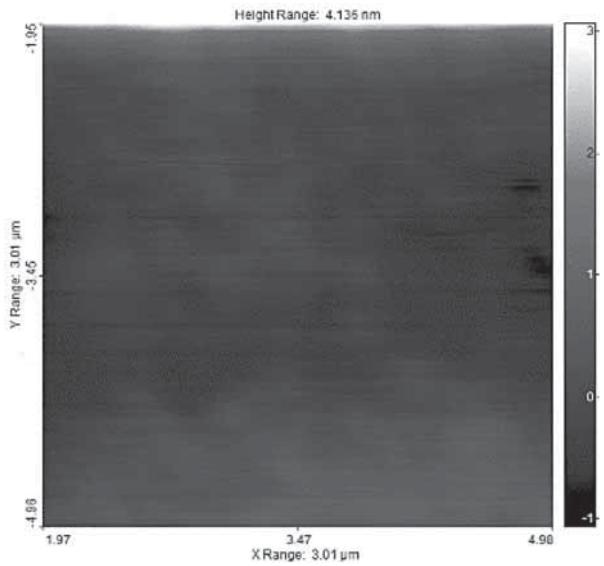

Figure 25. 2D image plots of Sample S102.

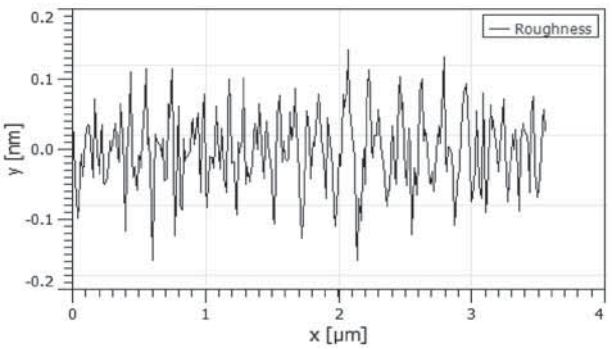

Figure 26. Roughness profile for Sample S102.

Taking into consideration all the previous issues, improvements were made in the ramping temperatures (R_1, R_2) and in the thermalization time (H_1) and soaking time (H_2). The results (Table 2) are seen in Samples S102 and S105. These samples have the best possible surface parameters obtained using this thermal-forming process. Sample S105 was prepared by forming the glass on the convex side of the quartz mandrel. Though its edges were flattened as compared to the glass sheets formed on the concave side, it still maintains a good figure in the central region which will eventually be used as a reflecting surface.

7. Conclusions

We have successfully carried out the thermal-forming process applicable to thin sheets of borosilicate glass, which can be used to produce optics for future hard X-ray telescopes. Such a technology has been shown to produce low-cost segmented X-ray mirrors, with excellent reflectance and scattering properties (Jimenez-Garate *et al.* 2003).

It is observed that the thermal-forming process preserves the micro-roughness and other surface properties of the raw glass sheet. The glass formed using the concave side of the quartz mandrel was not allowed to fully settle on the mandrel. This can be useful to achieve good surface parameters in case the surface specifications of the quartz mandrel are not up to the desired quality. The mandrel only serves as a guide surface for the lateral edges of the glass. In contrast to this, the thermally-formed glass using the convex side of the quartz mandrel showed better surface parameters. In future research, it is desirable to use a figured mandrel as a true master. Fixing the forming parameters, the stress-free glass sheets were produced with consistency.

For future hard X-ray missions, use of thermally-formed glass sheets will offer the best performance with minimum production time, cost and weight. Such substrates do not require polishing of the surface, to be coated with a reflecting material.

Acknowledgements

The authors would like to thank Mr Harshit Shah, Mr Vishwas Risbud, Mr Vilas Mhatre, Mr Jayprakash Koyande and Mr Balu Bagade, the staff of DAA, TIFR, for their contribution in the experimental work carried out in the X-ray laboratory, TIFR. They specially acknowledge the efforts of former staff member of DAA, TIFR, Mr Umesh Tonpe for his valuable contribution in the initial experiments of thermal slumping. They thank Prof. Shriganesh Prabhu and Prof. Venu Gopal Achanta, DCMP, TIFR for providing them with AFM facility in their laboratories time and again. They thank Prof. Pushan Ayyub, DCMP, TIFR for providing the SEM facility in his laboratory. They also thank Ms Bhagyashri Chalke, Mr Rudheer Bapat, Mr John Jesudasan, Mr Vivas Bagwe and Mr Gajendra Mule, staff of DCMP, TIFR and Dr Raghunandan Shukla, DHEP, TIFR for their valuable assistance in handling the SEM and AFM facilities. Finally, they also thank Mr Shirish Pathare, HBCSE, for providing his laboratory facility to perform polarimetric stress measurements for slumped glass sheets.

References

Agrawal P C *et al.* 2017, J. Astrophys. Astron., 38(2), 1

Aschenbach B. 2009, Exp. Astron., 26(1–3), 95

Burrows D. N. *et al.* 2005, Space Sci. Rev., 120(3), 165

Jansen F., Lumb D., Altieri B., Clavel J., Ehle M., Erd C., Gabriel C., Guainazzi M., Gondoin P., Much R., Munoz R., Santos M., Schartel N., Texier D., Vacanti G. 2001, The Spacecraft and Operations, A&A, 10, 61

Jahoda E. H., Keith; Swank J. H., Giles A. B., Stark M. J., Strohmayer T., Zhang W., Morgan E. H. 1996, Proc. SPIE, 2808, 59

Jimenez-Garate M. A., Charles J. H., William W. C., Finn E. C. 2003, Appl. Optics, 42(4), 724

Koglin J. *et al.* 2009, NuSTAR Hard X-Ray Optics Design and Performance, in Proceedings of SPIE—The International Society for Optical Engineering 7437

Mao P. 2002, Hard X-Ray Observations of the Extragalactic Sky: The High Energy Focusing Telescope and the Serendipitous Extragalactic X-Ray Source Identification Survey Thesis

Mao P. H., Harrison F. A., Windt D. L., Christensen F. E. 1999, Appl. Optics, 38(22), 4766

Martin C. W., Harvey D. T., Leon P. Van Speybroeck, Stephen L. O'Dell. 2000, Chandra X-Ray Observatory (CXO): Overview, in SPIE 4012, X-Ray Optics, Instruments and Missions III, 2 (July 18, 2000)

Orr J. F., Finlay J. B. 1997, Photoelastic stress analysis in: Optical Measurement Methods in Biomechanics, eds J. F. Orr and J. C. Shelton, Boston, MA: Springer, US, pp. 1–16

Pye L. D., Angelo M., Innocent J. 2005, Properties of Glass-Forming Melts

Sagdeo A. *et al.* 2010, Exp. Astron., 28(1), 11

Schott A. G., 2013, D 263® T Eco Thin Glass

Serlemitsos P. J., Peter J. *et al.* 2007, The X-ray telescope onboard Suzaku, Publ. Astron. Soc. Japan, 59(sp1), S9

Singh K. P. *et al*. 2014, ASTROSAT Mission, in SPIE 9144, Space Telescopes and Instrumentation: Ultraviolet to Gamma Rays

Singh K. P. *et al.* 2016, In-orbit performance of SXT aboard AstroSat, in: Proceedings SPIE 9905, Space Telescopes and Instrumentation 2016: Ultraviolet to Gamma Ray, 99051E (18 July 2016); https://doi.org/10.1117/12.2235309

Singh K. P. *et al.* 2017, Soft X-ray focusing telescope aboard AstroSat: Design, characteristics and performance J. Astrophys. Astron., 38(2), Art ID 29

Singh K. P. 2015, AstroSat: India's First Multi-Wavelength Astronomy Satellite, in National Conference on CICA-HEP, Dibrugarh (2015) pp. 1–6

Singh K. P. 2005, Resonance, 10(6), 15

Sørensen B. E. 2014, Eur. J. Mineral., 25(6), 1041

Tanaka Y., Inoue H., Holt S. S. 1994, The X-Ray Astronomy Satellite ASCA, Publ. Astron. Soc. Jpn., 46(3), L37

Wang W *et al*. 1992, Digital photoelastic analysis of stress distribution in a castable, ceramic crown with different margin designs, in: Experimental Mechanics, ed. E. G. Little, Elsevier, Amsterdam, pp. 467–476

Windt D. L., Waskiewicz W. K., Griffith J. E. 2009, Appl. Optics, 33(10), 2025

Wolter V. H. 1961, Spiegelsysteme Streif Enden Ein f Alls Als Abbildende Optiken Fiir Rijntgenstrarirlen 1, September